KLF Analysis Report: Hyperon Spectroscopy Simulation Studies

Mikhail Bashkanov and Nicholas Zachariou

University of York, Heslington, York YO10 5DD, UK

Kijun Park and Simon Taylor

Thomas Jefferson National Accelerator Facility, Newport News, VA 23606, USA

Igor Strakovsky

Institute for Nuclear Studies, Department of Physics,
The George Washington University, Washington, DC 20052, USA
(Dated: March 2020)

PACS numbers:

Abstract

We present Supplemental materials for hyperon spectroscopy simulation studies for the KLF proposal addressed to PAC48.

Contents

I. INTRODUCTION

The present experimental knowledge of the spectra of hyperons remains remarkably incomplete. A newly proposed K_L-facility aim to measure the differential cross sections and the self-polarization of hyperons with the GlueX detector to enable precise partial wave analysis (PWA) in order to determine all the resonances up to 2500 MeV in the spectra of the Λ, Σ, Ξ, and Ω hyperons.

Several simulations on various channels were performed to obtain an insight on the expected results and the beam time requirements for precision measurements. The simulations results that follow are based on a 100 days of beamtime with a 1×10^4 K_L/s impinged on a 40 cm long target. Generated events assuming standard beam/target conditions are processed through a full Geant3-based Monte Carlo (MC) simulation of the GlueX detector. Below we provide a summary of studies performed on various channels for Hyperon spectroscopy.

An extensive list of channels was generated and studied in great detail. Here we focus on simulations for the following channels:

1. $K_L p \rightarrow K_s p$

2. $K_L p \rightarrow \pi^+ \Lambda$

3. $K_L p \rightarrow K^+ \Xi^0$

4. $K_L n \rightarrow K^+ \Xi^-$

5. $K_L n \rightarrow K^+ \Xi^{*-}$

6. $K_L p \rightarrow K^+ n$

These reactions represent key measurements and correspond to typical kinematic conditions at KLF. The $K_s p$ and $\Lambda \pi^+$ are the main reaction channels to study Σ^* resonances in the s-channel (analogue of $N\pi$ in nucleon N^* case). The $K^+ \Xi^0$ reaction also aim at Σ^* s-channel production for the resonances which does not couple to elastic channels strongly, an analogue of $N^* \rightarrow \Lambda K$ reactions. The $K^+ \Xi^-$ reactions demonstrate our ability to measure reactions on neutron target as well as ability to access $\Lambda^* - \Sigma^*$-mixed channel. The $K^+ \Xi^{*-}$ channel show ability to measure excited cascade states in associated production. And the $K^+ n$ channel demonstrate our ability to handle non-resonant background reactions properly. Combined, these reactions represent a core part of the KLF experimental program.

II. K_L BEAM

The K_L beam is generated by sampling the momentum distribution of K_L particles produced by interactions of a photon beam with a beryllium target 24 m upstream of the LH$_2$/LD$_2$ cryogenic target. The K_L beam profile was simulated to be uniform within a $\varnothing 0.06$ m at the LH$_2$/LD$_2$ cryogenic target. The expected K_L beam nonuniformity is below 2 % with a beam divergence $< 0.15°$ (see Table I). Due to the very strong t-dependence in the ϕ photoproduction cross section [2] and the P-wave origin of the $\phi \rightarrow K_L K_S$ decay, the majority of kaons will be produced at very small angles. In the simulation studies discussed in this section, 1×10^4 K_L/s are impinged on a 0.40 m long LH$_2$ target for a beamtime of 100 PAC days.

TABLE I: Expected electron/photon/kaon beam conditions at the K_L experiment.

| Property	Value
Electron beam current (μA)	5
Electron flux at CPS (s^{-1})	3.1×10^{13}
Photon flux at Be-target $E_\gamma > 1500$ MeV (s^{-1})	2.6×10^{11}
K_L beam flux at cryogenic target (s^{-1})	1×10^4
K_L beam σ_p/p @ 1 GeV/c (%)	~ 1.5
K_L beam σ_p/p @ 2 GeV/c (%)	~ 5
K_L beam nonuniformity (%)	< 2
K_L beam divergence (°)	< 0.15
$K^0/\overline{K^0}$ ratio at cryogenic target	2:1
Background neutron flux at cryogenic target (s^{-1})	6.6×10^5
Background γ flux at cryogenic target (s^{-1}), $E_\gamma > 100$ MeV	6.5×10^5

III. THE GLUEX DETECTOR
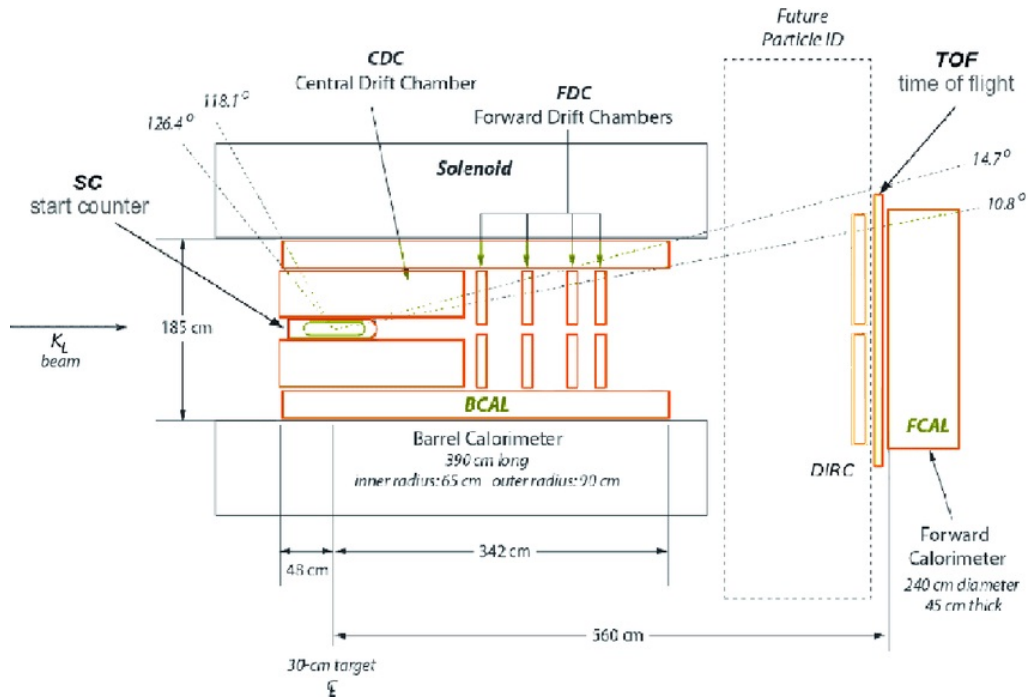
FIG. 1: Schematic view of the GlueX detector.

The GlueX detector is a large acceptance detector based on a solenoid design with good coverage for both neutral and charged particles [3]. The detector consists of a solenoid magnet enclosing devices for tracking charged particles and detecting neutral particles, and a forward region consisting of two layers of scintillators (TOF) and a lead-glass EM calorimeter (FCAL). A schematic view of the GlueX detector is shown in Fig. 1. The magnetic field at the center of the bore of the magnet for standard running conditions is about 2 T. The trajectories of charged particles produced by interactions of the beam with the 0.40-m LH_2/LD_2 cryogenic target at the center of the bore of the magnet are measured using the Central Drift Chamber (CDC) for angles greater than $\approx 20°$ with respect to the beamline Forward-going tracks are reconstructed using the Forward Drift Chambers (FDC). The timing of the interaction of the kaon beam with the LH_2 cryogenic target is determined using signals from the SC [4], an array of 30 mm thin (3 mm thick) scintillators enclosing the target region. Photons are registered in the central region by the BCAL [5]. Detector performance and reconstructions techniques were evaluated during the main GlueX program. Details can be found elsewhere [6].

The following sections provide details on particle identification as well as details on the various channels studied. All simulations assumed standard beam/target conditions listed in Table I. A Geant3 based simulation of the GlueX detector was used to process all generated events.

IV. PARTICLE IDENTIFICATION

For each channel, one primary particle (the proton for the $K_S p$ channel, the π^+ for the $\pi^+\Lambda$ channel and the K^+ for the $K^+\Xi$ and K^+n channels) provides a rough determination for the position of the primary vertex along the beamline that is used in conjunction with the SC to determine the flight time and path of the K_L from the beryllium target to the hydrogen target, and thus determine its momentum. Protons, pions, and kaons are distinguished using a combination of dE/dx in the chambers and time-of-flight to the outer detectors (BCAL and TOF). The energy loss and timing distributions for the $K_S p$ channel are shown as an example in Fig. 2; the distributions are similar for the $\pi^+\Lambda$ channel, where a proton band arises from the $\Lambda \to \pi^- p$ decay. Also shown is the dE/dx distribution for the $K^+\Xi^0$ channel, where a prominent kaon band can be seen, along with pion and proton bands arising from Λ decays.

Since the GlueX detector has full acceptance in ϕ for charged particles and large acceptance in θ (roughly $1° - 140°$), a full reconstruction of events is feasible for the majority of the channels. That will allow to apply four or more
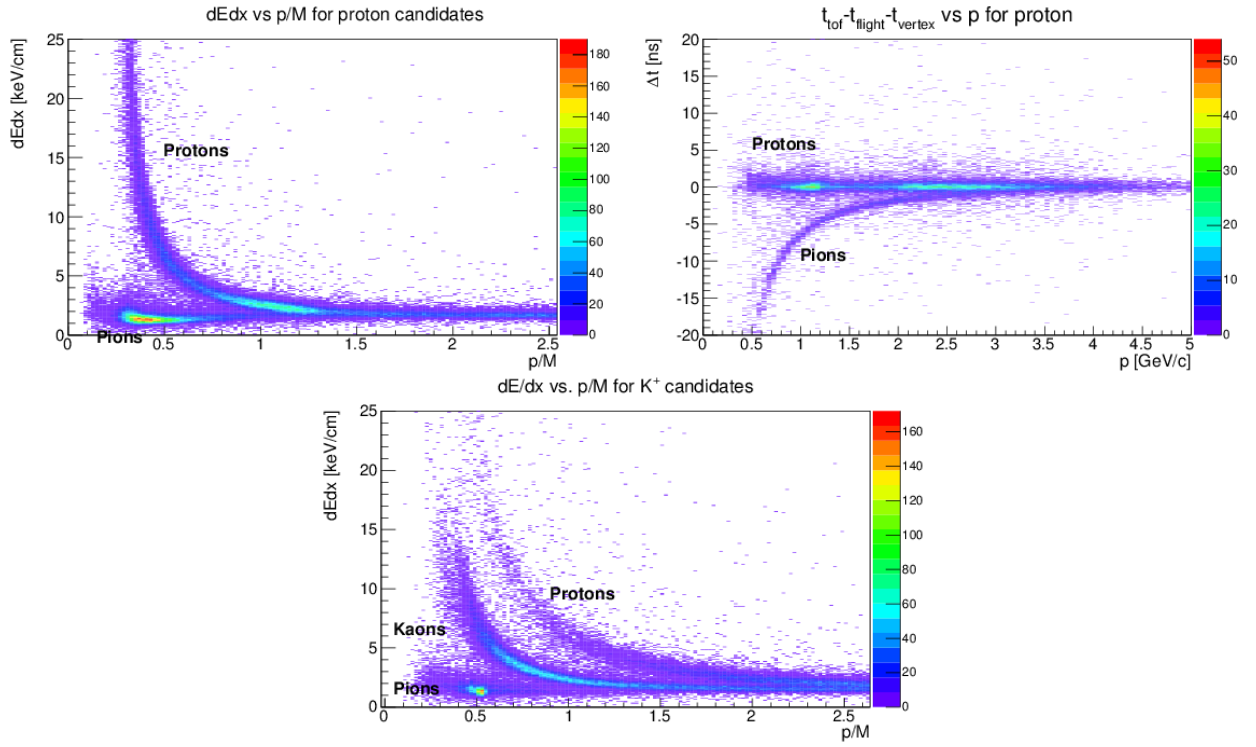
FIG. 2: Particle identification. Top left panel: dE/dx for the $K_S p$ channel. Top right panel: Time difference at the primary "vertex" for the proton hypothesis for the $K_S p$ channel using the TOF. Bottom panel: dE/dx for the $K^+\Xi$ channel. The proton and pion bands arise from the decay of the Λ.

overconstrain kinematical fit and improve the resolution considerably. A typical comparison between W reconstruction using the K_L-momentum for 250 psec SC resolution (red dots) and the other using kinematically fitted final-state particles for the $K_S p$ channel (blue dots) is shown in Fig. 3. Detection of all final state particles in any channel allows an improvement by about an order of magnitude in the W resolution at high W.
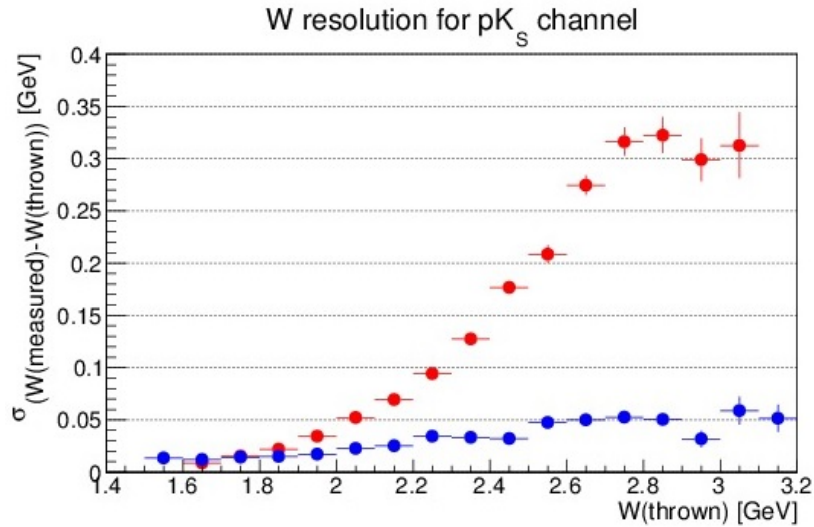

FIG. 3: W resolution for the $K_S p$ channel, (blue dots) using kinematic fitting after reconstruction of all final state particles; (red dots) using K_L time-of-flight.
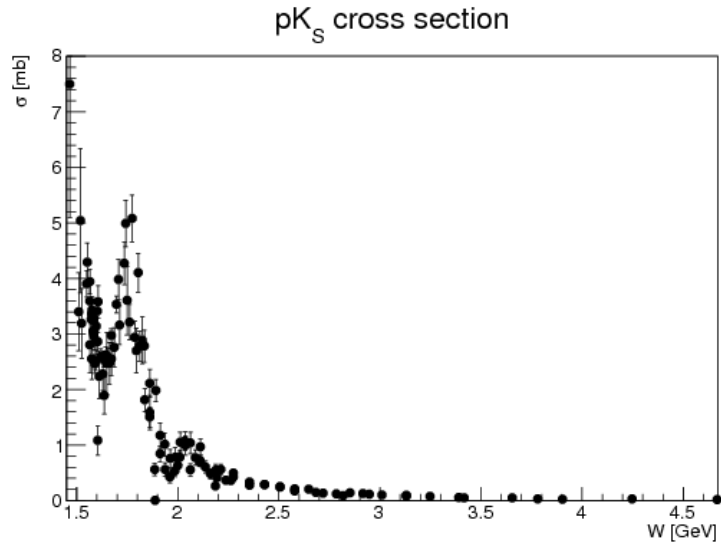
V.   DETAILS OF MC STUDY FOR $K_L p \to K_S p$

FIG. 4: Total cross section for $K_L p \to K_S p$ as a function of W. The measured data are from [7] and references therein.

The total production cross section, shown in Fig. 4, is reasonably large; however, for the differential cross section there is a fair amount of tension in the existing data sets between different measurements, and the angular coverage in some bins is sparse. Figure 5 shows the existing differential cross section data for several bins in W. The cross section as a function of CM $\cos\theta$ was parametrized using a set of Legendre polynomials (blue curves in Fig. 5); the weights of each polynomial in the set depended on W. This parametrization was used to generate $K_L p \to K_S p$ events that were passed through a full Geant3-based Monte Carlo (MC) of the GlueX detector. The final-state particles were constructed using the standard GlueX reconstruction code. We reconstructed the K_S taking advantage of the BR of 69.2 % for $K_S \to \pi^+\pi^-$ [8]; the invariant mass of the $\pi^+\pi^-$ pair and W as computed from the four-momenta of the proton and the two pions is shown in Fig. 6.

After combining the four-momenta of the final-state particles with the four-momenta of the beam and the target, the missing-mass squared for the full reaction should be zero, which is also shown in Fig. 6. Finally, one requires conservation of energy and momentum in the reaction by applying a kinematic fit to the data.

After applying a 0.1 cut on the confidence level of the fit, an estimate for the reconstruction efficiency has been calculated and is shown as a function of W in Fig. 7. Here the efficiency includes the BR for $K_S \to \pi^+\pi^-$. The average reconstruction efficiency is about 7 %.

The statistical uncertainties in measured cross section for 100 days of running as a function of CM $\cos\theta$ for several values of W are shown in Fig. 8. We estimate that for $W < 3$ GeV, we will detect on the order of 2.7M $K_S p$ events in the $\pi^+\pi^-$ channel.
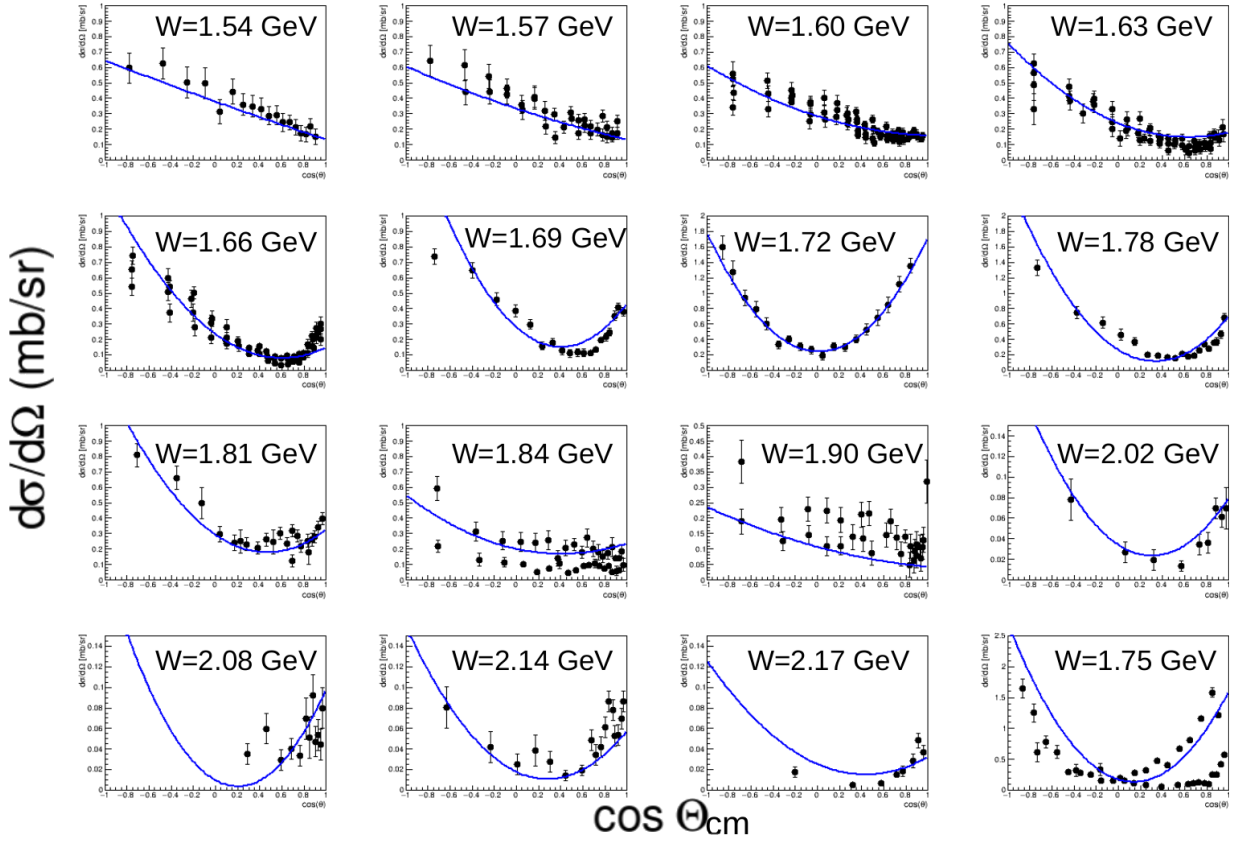
FIG. 5: Differential cross section plots for $K_L p \rightarrow K_S p$ as a function of W. The blue curves are the result of a parametrization of the cross section in terms of Legendre polynomials. The measured data are from [7].
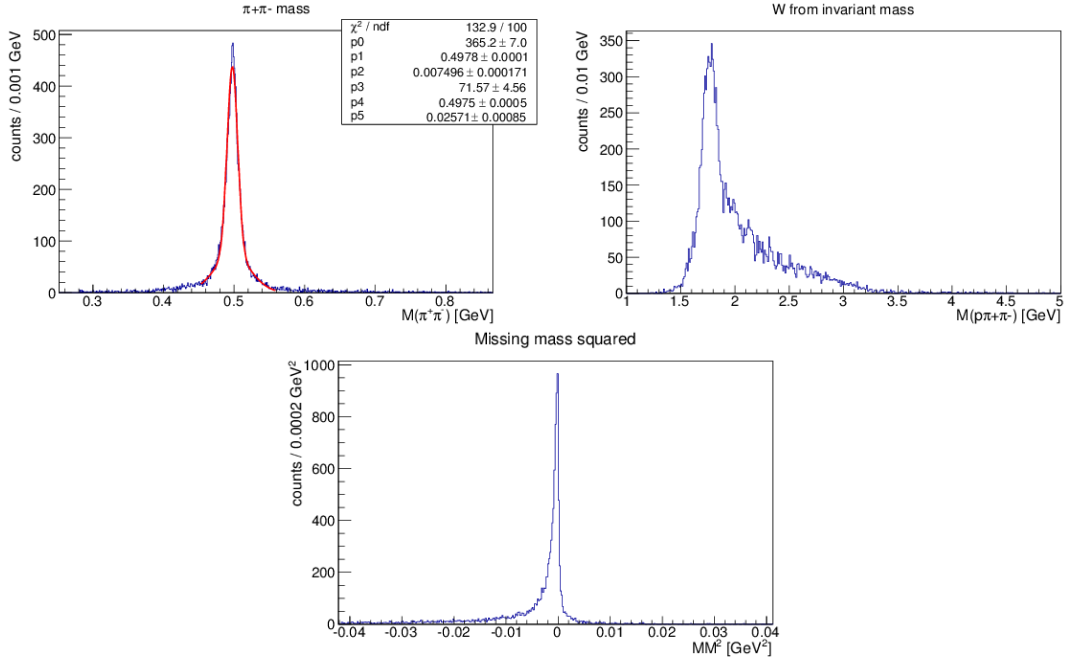

FIG. 6: Full reconstruction for $K_L p \rightarrow K_S p$ and $K_S \rightarrow \pi^+ \pi^-$. <u>Top left panel</u>: $\pi^+ \pi^-$ invariant mass. <u>Top right panel</u>: W computed from $\pi^+ \pi^- p$ invariant mass. <u>Bottom panel</u>: Missing-mass squared for the full reaction.
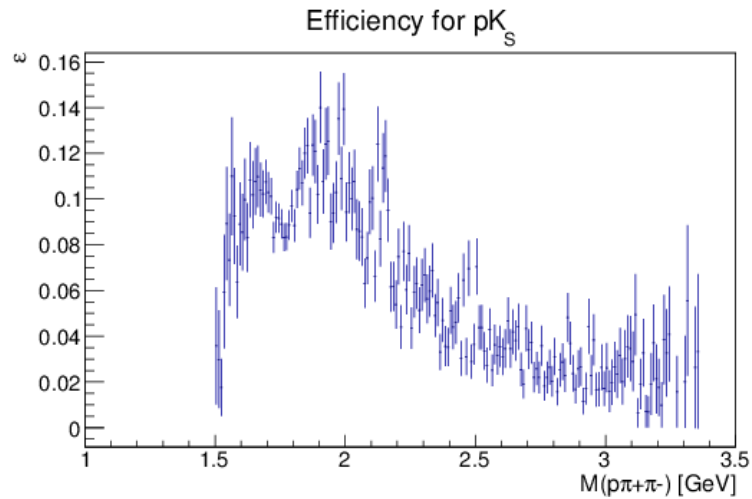
FIG. 7: Estimate the efficiency for full reconstruction of the $K_L p \to K_S p$ and $K_S \to \pi^+ \pi^-$ reaction chain as a function of W.
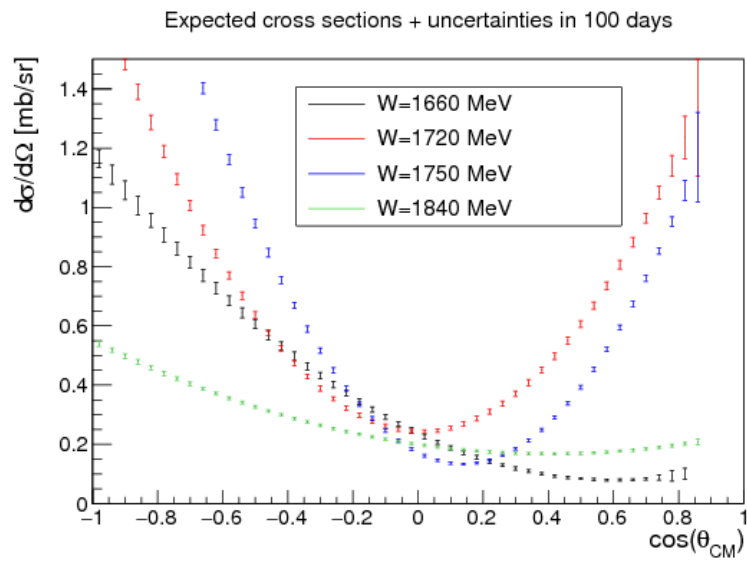

FIG. 8: Reconstructed $K_L p \to K_S p$ differential cross sections for various values of W for 100 days of running.

VI. DETAILS OF MC STUDY FOR $K_L p \rightarrow \pi^+ \Lambda$

The $K_L p \rightarrow \pi^+ \Lambda$ and $K_L p \rightarrow \pi^+ \Sigma^0$ reactions are key to studying hyperon resonances – an analog of $N\pi$ reactions for the N^* spectra. They are also the key reaction to disentangling the weak exchange degeneracy of the $K^*(892)$ and $K^*(1420)$ trajectories. (A general discussion is given in Ref. [1]). The first measurement of this reaction was performed at SLAC in 1974 [9] for K^0 beam momentum range between 1 GeV/c to 12 GeV/c. The total number of $\pi^+ \Lambda$ events was about 2500 events, which statistically limits the measurement.

For our proposed KL Facility at Hall-D, we expect a great increase in the statistics of $K_L p \rightarrow \pi^+ \Lambda$ for a very wide range of K_L beam momentum. Figure 9 shows the K_L beam momentum distributions from the generated counts (left) and reconstructed counts (right) when requiring $\beta_{K_L} > 0.95$ in time-of-flight.
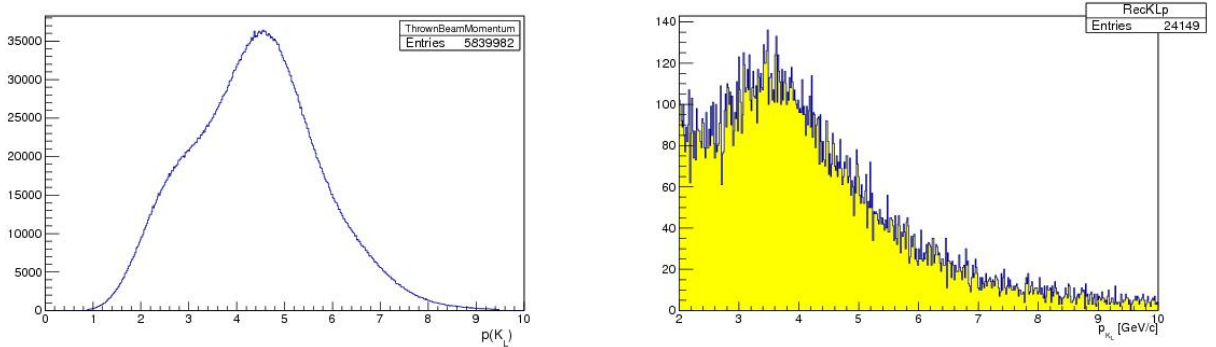

FIG. 9: Beam particle (K_L) momentum distribution in MC simulation, <u>Left panel</u>: Generated. <u>Right panel</u>: Reconstructed.

We have generated the $K_L p \rightarrow \pi^+ \Lambda$ reaction taking into account the realistic K_L beam momentum distribution in the event generator. This momentum spectrum is a function of the distance and angle. Events were processed through the standard Hall-D GEANT simulation with GlueX detector and momentum smearing and utilized JANA for particle reconstruction that was simulated.

Figure 10 shows a sample plot for polar angle versus momentum distribution of π^+, π^-, and protons from the generated event (left) and reconstructed event (right).

Figure 11 shows an example of the reconstructed the Λ invariant mass (left) and missing mass (right). We obtained a 5 MeV invariant-mass resolution and a 150 MeV missing-mass resolution and estimateed the expected total number of $\pi^+ \Lambda$ events as final-state particle within topology of $1\pi^+$, $1\pi^-$, and 1 proton. In 100 days of beam time with 1×10^4 K_L/s on the liquid hydrogen target, we expect to detect around 5.3M $K_L p \rightarrow \pi^+ \Lambda$ events for $W < 3$ GeV. Such an unprecedented statistics will improve our knowledge of these states through PWA.

The $K_L p \rightarrow \pi^+ \Lambda$ reaction has a relatively high production cross section the order of a few mb in our proposed K_L-momentum range (1 – 6 GeV/c). The beam resolution has been calculated at the time-of-flight vertex time resolution (250 psec) of the start counter (TOF-ST). The estimates of the statistical uncertainty of the $\pi^+ \Lambda$ total cross section as a function K_L beam momentum with GlueX detector in Hall D are shown in Fig. 12 (left). We kept the same momentum bin size as the one from the SLAC data. The box-shaped error bars in the MC points (red triangles) were increased by a factor of 10 for comparison with the SLAC data. The proposed measurements will provide unprecedented statistical accuracy to determine the cross section for a wide range of K_L-momentum. In Fig. 12 (right), the t-dependent cross sections were shown in three beam momentum bins same as SLAC data sets: $p_{K^0} = 1.5 – 2.5$ GeV/c (solid bullets), $p_{K^0} = 2.5 – 3.5$ GeV/c (solid rectangles)and $p_{K^0} = 3.5 – 5.0$ GeV/c (solid triangles). As it shows, a strong forward peaking in t-channel for all momenta was observed, which appears to move out —-t— = 0.4 - 0.5 GeV^2 at higher momenta.

Parity violation in the weak decay of Λ makes it possible to measure the induced polarization. The induced Λ polarization (P_Λ) can be observed by measuring the angular distribution of the proton with respect to the normal vector to the production plane. The recoil polarization is extremely sensitive and valuable tool to constrain PWA amplitudes. Our simulations show that existing SLAC data can be improved a lot by K_L facility at JLab (see Fig. 13).

The major source of systematic uncertainty for this reaction would be a particle miss-identification among π^+, K^+, and protons in the final state. However, requiring the reconstructed Λ and side-band subtraction technique for background will reduce contributions from misidentified events substantially.
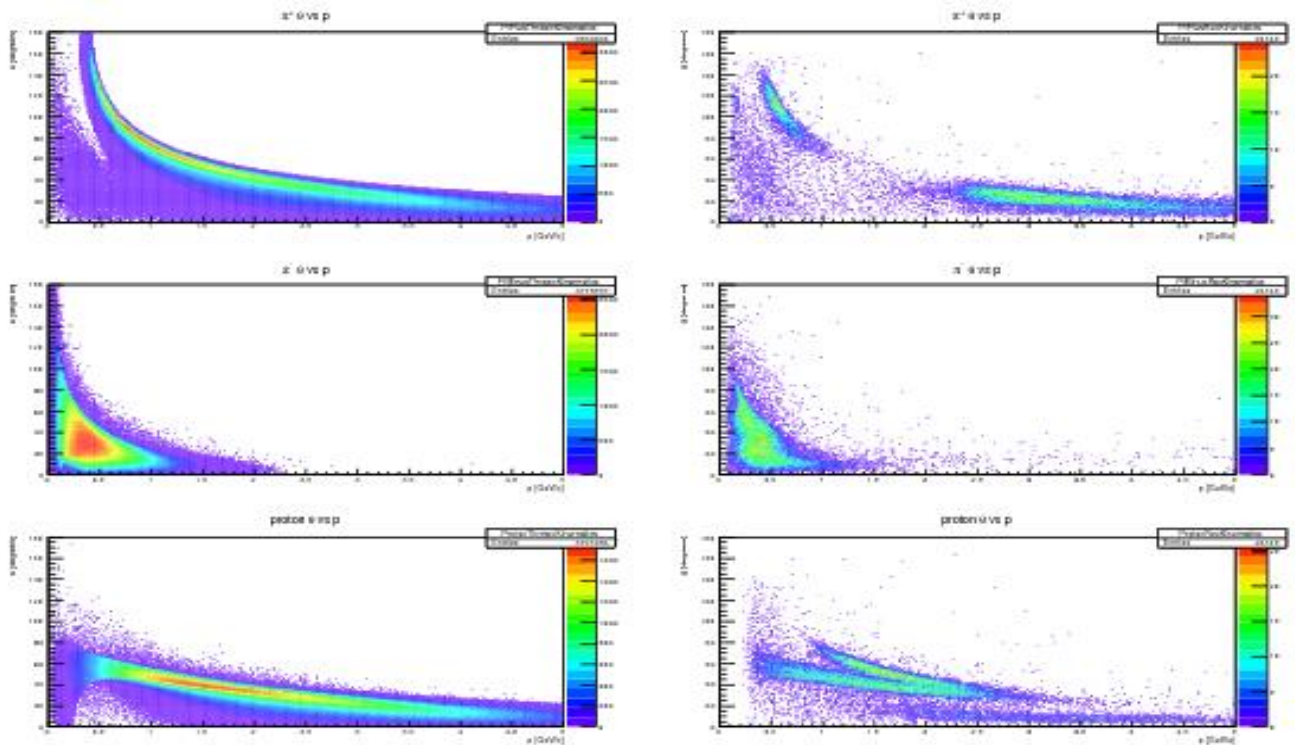
FIG. 10: Momentum and angular distributions. Top row panel: π^+, Middle row panel: π^-, Bottom row panel: proton. Left column panels: Generated and Right column panels: Reconstructed events.
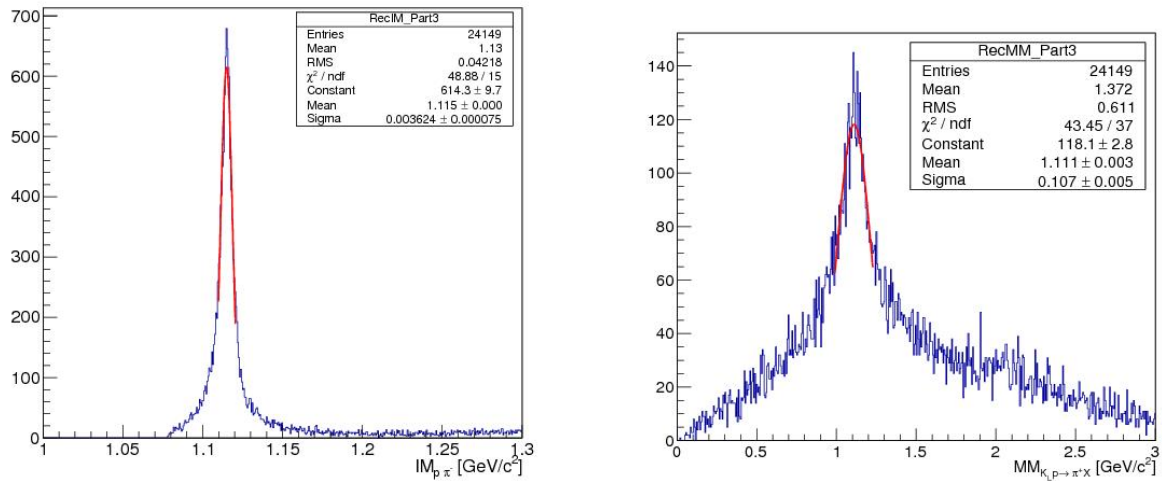

FIG. 11: Λ invariant-mass distribution reconstructed. Left panel: From its $\pi^- p$ decay particles. Right panel: Missing mass of $\pi^+ X$ (right).
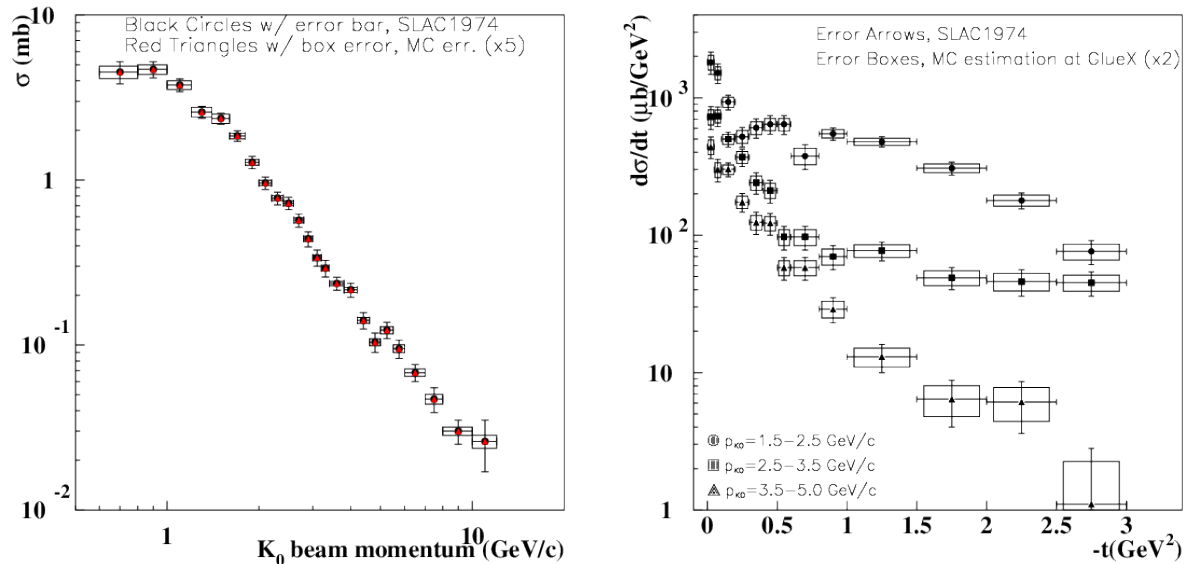
FIG. 12: Left panel: Total cross section uncertainty estimate (statistical uncertainty only) for $K_L p \to \pi^+ \Lambda$ reaction as a function of K_L beam momentum in comparison with SLAC data [9]. The experimental uncertainties have tick marks at the end of the error bars. The box-shaped error bars in the MC points from K_L beam at GlueX were increased by a factor of 5. Right panel: t-dependent cross sections in three beam momentum bins (same as SLAC data sets): $p_{K^0} = 1.5 - 2.5$ GeV/c (solid bullets), $p_{K^0} = 2.5 - 3.5$ GeV/c (solid rectangles), and $p_{K^0} = 3.5 - 5.0$ GeV/c (solid triangles). The box-shaped error bars in the MC points from K_L beam at GlueX detector were increased by a factor of 2.
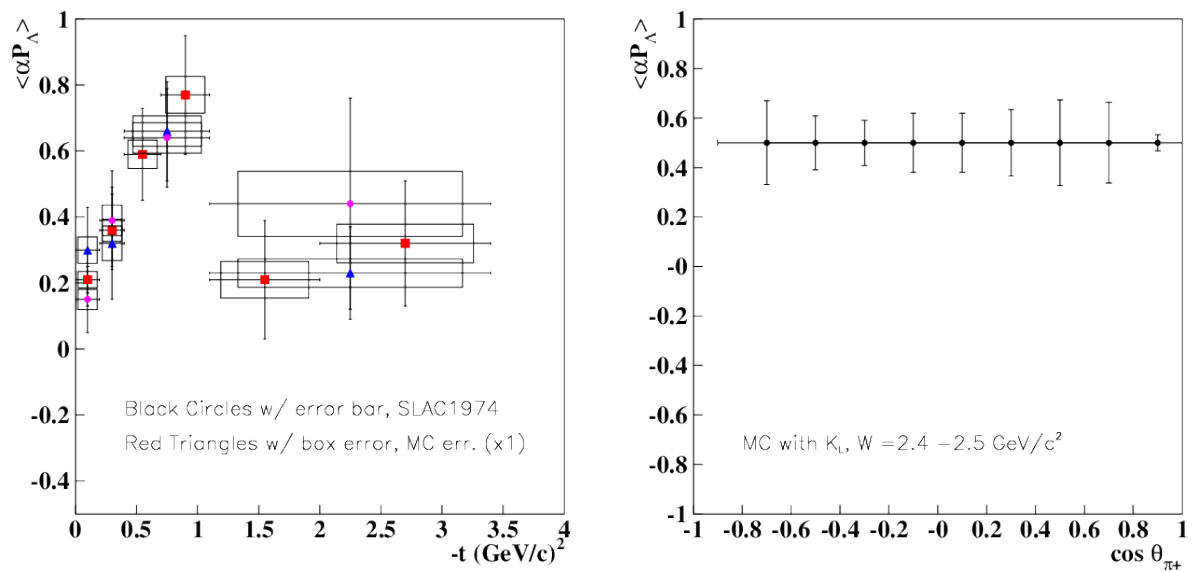

FIG. 13: Left panel: Averaged polarization, $\langle \alpha P_\Lambda \rangle$ as a function of t from Ref. [9], $p_{K^0} > 2.5$ GeV/c (red boxes), $p_{K^0} = 2.5 - 3.8$ GeV/c (blue triangles) and $p_{K^0} > 3.8$ GeV/c (purple bullets). The experimental uncertainties have tick marks at the end of the error bars. The box-shaped error bars from the MC for the K_L beam at GlueX, assuming 100 days beamtime. $\alpha = 0.645$ is the Λ analysing power. Right panel: Estimates of the statistical uncertainties of the Λ polarization as a function of CM $\cos \Theta_{\pi+}$ for the $W = 2.4 - 2.5$ GeV energy bin.

VII.   DETAILS OF MC STUDY FOR $K_L p \to K^+ \Xi^0$ AND $K_L n \to K^+ \Xi^-$

The study of cascade data will allow us to place stringent constraints on dynamical coupled-channel models. It was recently found in N^* spectroscopy that many N^* resonances do not couple strongly to a $N\pi$ channel, but are nicely seen in $K\Lambda$ and $K\Sigma$ channels. The corresponding situation in hyperon spectroscopy leads to many Λ^* and Σ^* resonances decaying preferably to a $K\Xi$ channel (see Ref. [1] for details). In addition, cascade data will provide us with long-sought information on missing excited Ξ states and the possibility to measure the quantum numbers of the already established $\Xi(1690)$ and $\Xi(1820)$ from a double-moments analysis. The expected large data sample will allow us to determine the induced polarization transfer of the cascade with unprecedented precision, which will place stringent constraints on the underlying dynamics of the reaction. Polarization measurements of hyperons shed light on the contribution from individual quarks to the overall polarization of these states. The polarization of the ground-state cascade can be measured from its weak decay in a straightforward way. With a K_L beam, the study of the reactions $K_L p \to K^+ \Xi^0$ and $K_L n \to K^+ \Xi^-$ is quite simple and an unprecedented statistical sample can be easily obtained. The statistical uncertainty obtained for two-fold differential polarization observables with 100 days of beam time ($\sim 1 \times 10^5$ reconstructed events) is of the order of 0.05–0.1, which will allow precision tests on the underlying dynamics to be performed. It also will be a first measurement of this kind.

A. $\mathbf{K_L p \to K^+ \Xi^0}$:

The section here focuses on the reconstruction of $K_L p \to K^+ \Xi^0$ but the initial procedure for particle identification and reaction reconstruction is almost identical to the reaction on the neutron ($K_L n \to K^+ \Xi^-$). Three topologies can be used to reconstruct the reaction $K_L p \to K^+ \Xi^0$ on free proton targets. Topology 1 requires the detection of a K^+, topology 2 requires the detection of a K^+ and a Λ by utilizing its high branching ratio to a $\pi^- p$ pair (63.9 %), and Topology 3 requires the detection of the two-photon decay of the π^0 from $\Xi \to \pi^0 \Lambda$. Particle identification is done via a probabilistic approach involving dE/dX, time-of-flight, and track curvature information. The dE/dX distributions for kaon, proton, and π^- candidates are shown in Fig. 14.
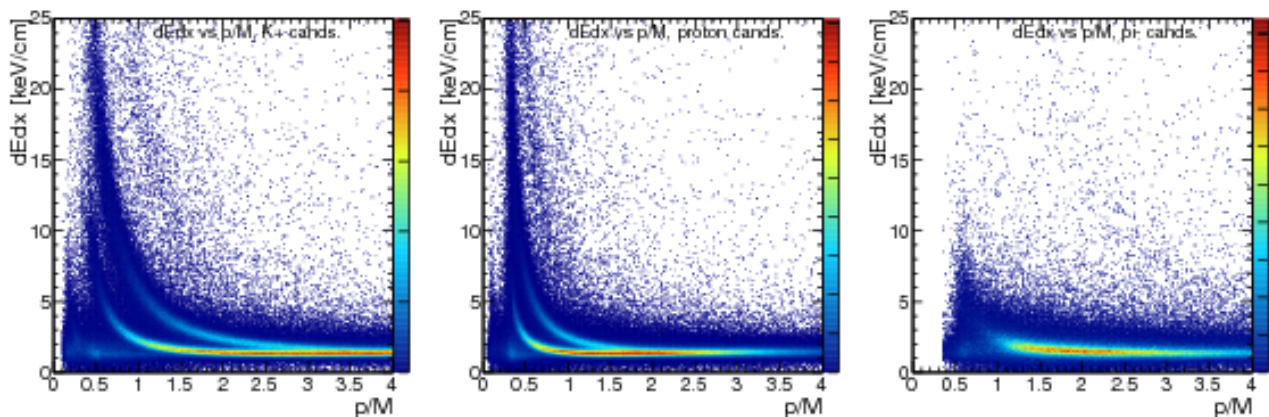

FIG. 14: dE/dX distributions used in kaon proton and π^- identification for the reconstruction of $K_L p \to K^+ \Xi^0$.

At low particle momenta, kaons and protons can be well separated, but high-energy particles cannot be unambiguously differentiated by dE/dX or by ToF information, which leads to particle misidentification. The higher the W, the higher ejectile energy and the more misidentification contributions we have. In this analysis (specifically Topology 2 and 3), these events were largely removed by making an invariant-mass cut on the $\pi^- p$ pair.

Figure 15 shows the missing mass of $K_L p \to K^+ X$ for simulated data for the reaction $K_L p \to K^+ \Xi^0$ used in the reconstruction of all topologies, the invariant-mass distribution of the $\pi^- p$ pair used to reconstruct Topology 2 ($K_L p \to K^+ \Lambda X$) and 3, and the invariant-mass of the two-photon pair used to reconstruct Topology 3 ($K_L p \to K^+ \Lambda \pi^0$). A 3σ cut on these distributions allows us to reconstruct the reaction fully. Fig. 15 (left) shows the 3σ W-dependent cut applied to select the missing Ξ^0 as well as the W-dependent 3σ cut to reconstruct the reaction $K_L p \to K^+ n$.

The latter is one of the major sources of background for our reaction for Topology 1; however, the missing-mass resolution (obtained with a vertex-time resolution of 250 psec) allows a clean separation of these two reactions up to W = 2.3 GeV Above this value, special treatment of the $K_L p \to K^+ n$ background is required as discussed later on.
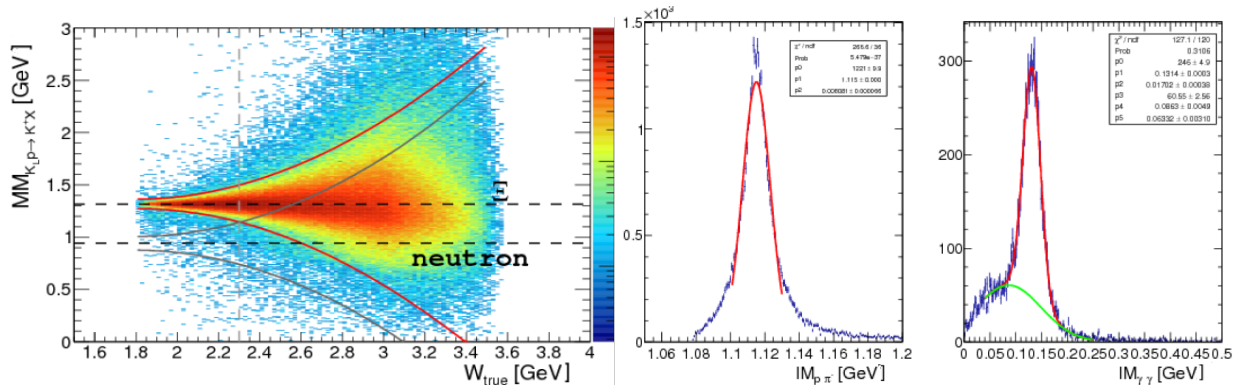
FIG. 15: Missing mass of the reaction $K_L p \to K^+ X$ used to reconstruct the reaction $K_L p \to K^+ \Xi^0$ (Topology 1), the invariant mass of $p\pi^-$ pair (Topology 2), and the invariant mass of the two-photon pair (Topology 3).

The detection efficiency as a function of the true W for each topology for the reaction on the proton is shown in Fig. 16. As expected, the efficiency is highest for Topology 1 reaching a maximum at 60 % for W = 2.05 GeV. The efficiency for Topology 2 is about an order of magnitude less than Topology 1, and Topology 3 detection efficiency is on average 0.8 %. The efficiency for the reaction on the neutron for a fully exclusive reaction is of the order of a few percent.
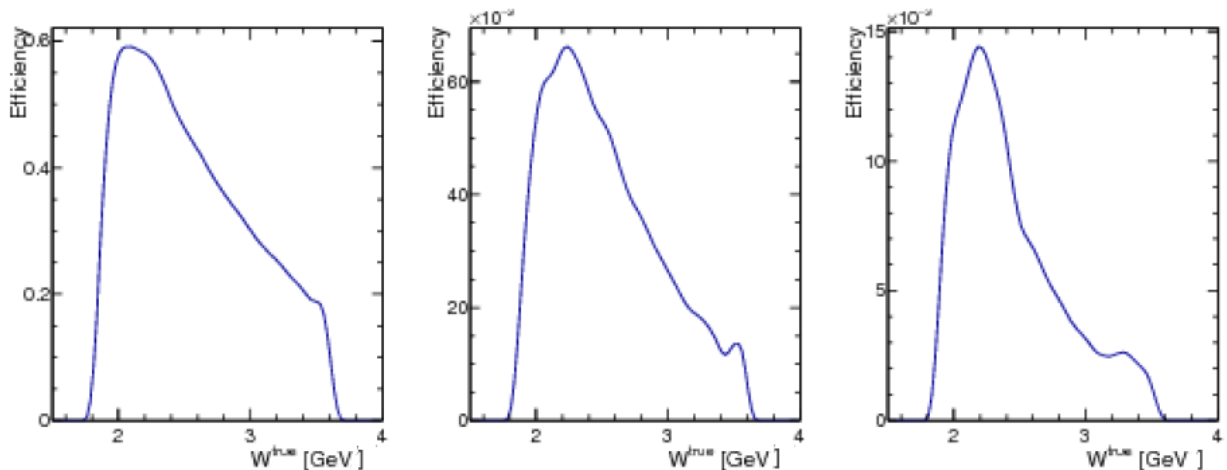

FIG. 16: Detection efficiency for the reaction $K_L p \to K^+ \Xi^0$ for each topology.

In 100 days of beamtime, we expect 3×10^6 $K_L p \to K^+ \Xi^0$ events. Out of which, one can reconstruct 2×10^6 events for Topology 1 ($K_L p \to K^+ X$); 1×10^5 for Topology 2 ($K_L p \to K^+ \Lambda X$); and 2×10^4 for Topology 3 ($K_L p \to K^+ \Xi^0$). Figure 17 compares the statistical uncertainties of the total and differential cross sections for the reaction $K_L p \to K^+ \Xi^0$ with existing data taken from [?] for the three different topologies (Column 1: only K^+ reconstructed, Column 2: $K^+ \Lambda$ reconstructed, and Column 3: $K^+ \Xi^0$ reconstructed).

Different sources of background will contribute in the three topologies used to study this reaction. Disentangling our signal $K_L p \to K^+ \Xi^0$ from the reaction $K_L p \to K^+ n$ (crucial for Topology 1), which has two orders of magnitude larger cross section is expected to be relatively straightforward. As mentioned before, a simple missing-mass cut is sufficient to remove any contributions from this reaction for $W < 2.3$ GeV. For $W > 2.3$ GeV, an s-weight approach (or neuralNets, etc.) can be utilized to remove these contribution as the shape of the background under any cascade events can be well established from simulations. Figure 18 shows the W-dependence of the missing-mass distribution of $K_L p \to K^+ X$ for the simulated reactions $K_L p \to K^+ \Xi^0$ and $K_L p \to K^+ n$ (left panel). The right panel shows the missing-mass projection at W = 1.9 GeV. In addition to $K_L p \to K^+ n$, the reaction $K_L p \to \pi^+ \Lambda$ is also a source of background events for Topology 1 ($K_L p \to K^+ X$) and 2 ($K_L p \to K^+ \Lambda X$). This channel contributes when the final-state π^+ is misidentified as a K^+. This shifts the missing mass of $K_L p \to \pi^+ X$ to values lower than the ones expected, which leads to a good separation of this source of background below $W < 2.2$ GeV. Figure 19 shows the missing-mass distribution of these misidentified events, which show similar distribution with $K_L p \to K^+ n$ events.
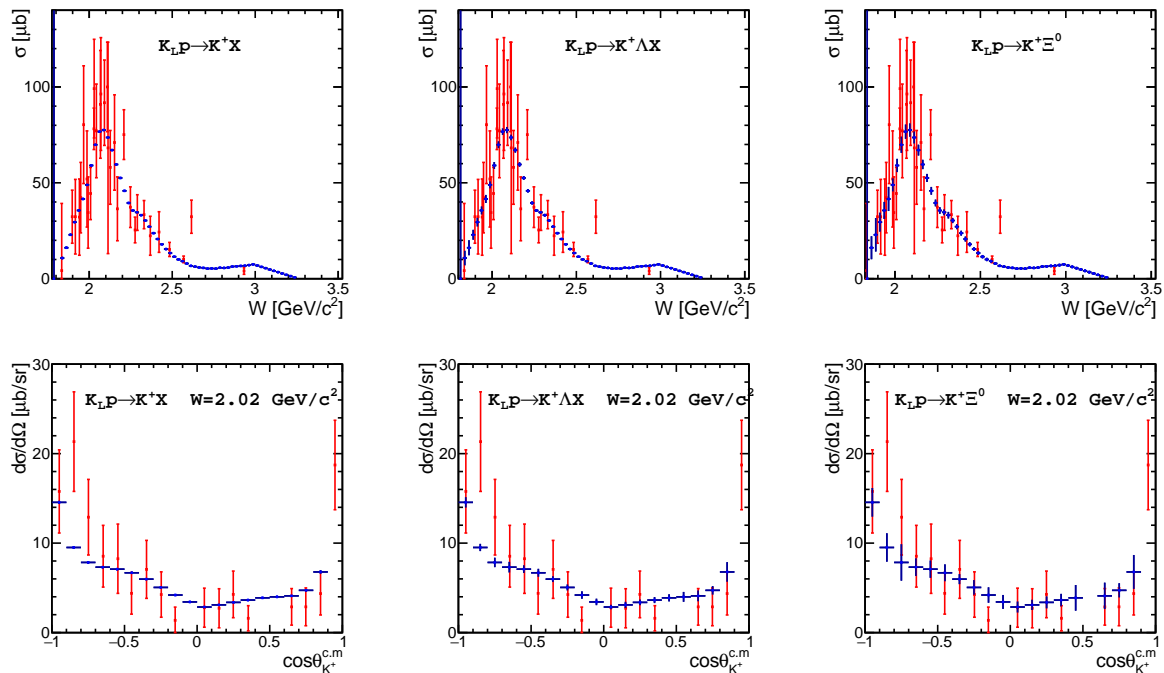
FIG. 17: Total and differential cross section statistical uncertainty estimates (blue symbols) for the three topologies (Column 1: only K^+ reconstructed, Column 2: $K^+\Lambda$ reconstructed, and Column 3: $K^+\Xi^0$ reconstructed) in comparison with data taken from Ref. [?] (red symbols).
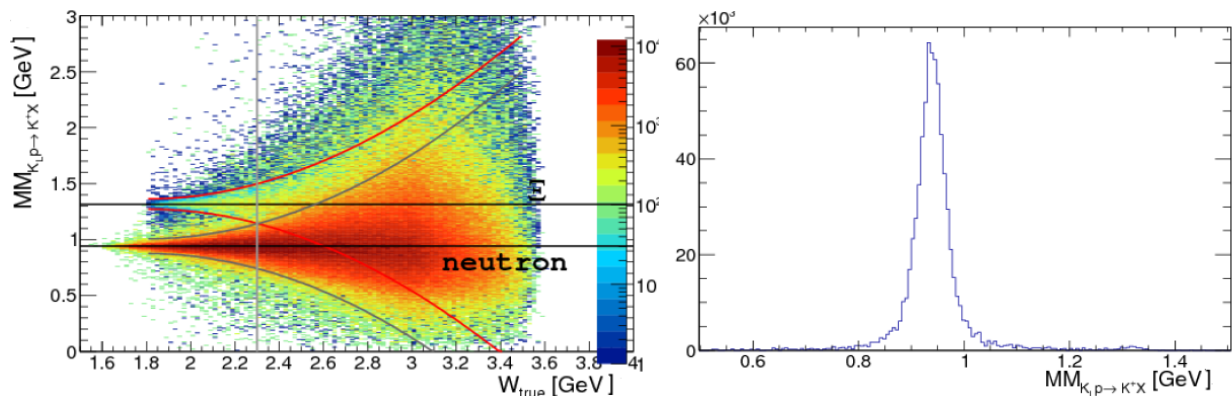

FIG. 18: Missing mass of the reaction $K_L p \to K^+ X$ used to reconstruct the reactions $K_L p \to K^+\Xi^0$ (Topology 1) and $K_L p \to K^+ n$ (which has about 2 orders of magnitude larger cross section). Right panel: shows the missing mass at W = 1.9 GeV.

Contributions from these events for Topology 3 is completely removed by the requirement of two photons in the final state that reconstruct the mass of π^0. For Topology 2, coplanarity cuts between the reconstructed (misidentified) K^+ and Λ can reduce contributions, where as a background subtraction approach using the missing-mass information can be used to remove any contribution at $W > 2.2$ GeV.

1. Ξ^0 Induced Polarization:

The expected statistics also allow us to determine the cascade-induced polarization by utilizing the fact that the cascade is self-analyzing with an analyzing power of -0.406 [8].
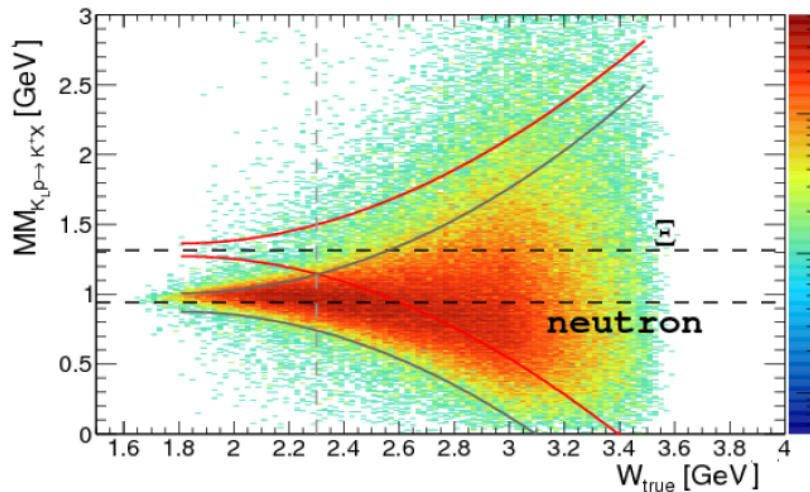
FIG. 19: Missing mass of the reaction $K_L p \to K^+ X$ for simulated events from the reaction $K_L p \to \pi^+ \Lambda$. The reconstructed events here results from a pion misidentified as a kaon.

In terms of four-vectors, conservation of energy and momentum for this reaction is written as follows:

$$\mathcal{P}_{K_L} + \mathcal{P}_p = \mathcal{P}_{K^+} + \mathcal{P}_{\Xi^0}. \tag{1}$$

The production plane is then defined by

$$\hat{y} = \frac{\vec{P}_\Xi \times \vec{P}_{K_L}}{|\vec{P}_\Xi \times \vec{P}_{K_L}|}. \tag{2}$$

The $\hat{z}$ axis lies along the beam direction

$$\hat{z} = \frac{\vec{P}_{K_L}}{|\vec{P}_{K_L}|}, \tag{3}$$

and thus the $\hat{x}$ axis is defined to give a right-handed coordinate system:

$$\hat{x} = \hat{y} \times \hat{z}. \tag{4}$$

The determination of P_Ξ^y can be established by linear fits to the acceptance-corrected pion angular ($\cos \theta_\pi^y$) yields. Fitting these distributions with a first-degree polynomial,

$$y = a_0(1 + a_1 \cos \theta_\pi^y), \tag{5}$$

allows the determination of a_1, which gives us the the induced polarization

$$a_1 = P_\Xi^y \alpha. \tag{6}$$

Alternatively, one can determine the induced polarization transfer from determining the forward-backward asymmetry, A^y, of the pion angular distribution. This asymmetry is defined as

$$A^y = \frac{N_+^y - N_-^y}{N_+^y + N_-^y}, \tag{7}$$

where N_+^y and N_-^y are the acceptance-corrected yields with $\cos \theta_\pi^y$ positive and negative, respectively. The asymmetry is related to the induced polarization by

$$P_\Xi^y = \frac{-2A^y}{\alpha}. \tag{8}$$

The statistical uncertainty in the asymmetry measurement of P_Ξ^y is related to the Poisson uncertainty in N_+^y and N_-^y. Propagating this uncertainty to the uncertainty of A^y gives

$$\sigma_{A^y} = \frac{2}{(N_+^y + N_-^y)^2} \sqrt{N_+^y N_-^y (N_+^y + N_-^y)}. \tag{9}$$

The uncertainty in P_Ξ^y is then found by propagating σ_{A^y} and σ_α:

$$\frac{\sigma_{P_\Xi^y}}{P_\Xi^y} = \sqrt{(\frac{\sigma_{A^y}}{A^y})^2 + (\frac{\sigma_\alpha}{\alpha})^2}. \tag{10}$$

The above procedure is identical to the case of Ξ^- where the angle $\cos\theta_\pi^y$ is given by the negative pion from the cascade decay, in the Ξ^- rest frame.

Figure 20 shows the statistical uncertainty estimates of the induced polarization of the cascade by simple fits to the acceptance-corrected yields of the pion angular distribution in the Ξ^0 rest frame.
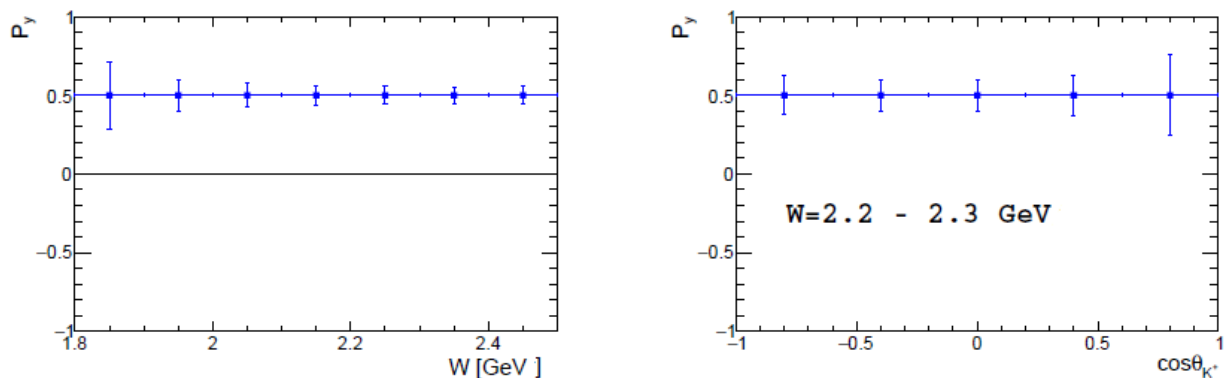

FIG. 20: Estimates of the statistical uncertainties of the induced polarization of the cascade in a $K_L p \to K^+ \Xi^0$ reaction as a Left panel: Function of W (one-fold differential). Right panel: Function of CM $\cos\theta_{K+}$ (two-fold differential).

B. $\mathbf{K_L p \to K^+ \Xi^-}$:

The analysis of this reaction on the neutron is based on the same approach as the one described above for $K_L p \to K^+ \Xi^0$. The main difference comes from the momentum distribution of the target nucleon. This issue can be easily addressed by selecting semi-exclusive events having only the spectator proton undetected. The analysis requires the detection of all final-state particles besides spectator, namely the K^+, the π^- from the cascade decay and the proton and π^- from the Λ decay. Even though this condition reduces the available statistics, the W resolution can be kept high.

The reconstruction of $K_L n \to K^+ \Xi^-$ follows closely the steps outlined for the reaction on the proton $K_L p \to K^+ \Xi^0$. The identification of the pions that originates from the Λ and Ξ decays is the main difference between the two channels. Fig. 21 (left) shows the invariant mass between the proton and one of the two detected pions. It is clear from this that the pion that originates from the Λ is easily identified with minimal combinatorial background.

The invariant mass of two pions and the proton is shown in Fig. 21 (right), clearly reconstructing the Ξ^- mass. Determination of cross sections and the induced polarization is identical to the $K_L p \to K^+ \Xi^0$ channel.

Based on the models described in Ref. [1] (Appendix. 3.12), polarized data on the reaction $K_L n \to K^+ \Xi^-$ were generated. In 100 days of beamtime, we expect to produce several million events (between 3 and 10) depending on the two available solutions, which give very different predictions. From this, the reconstruction of 7×10^4 or 3×10^5 events is expected for the fully exclusive reaction selection. In the same manner as the reaction on the proton ($K_L p \to K^+ \Xi^0$), we will utilize the fact the the cascade is self-analyzing with an analyzing power of -0.458 [8]. The statistical uncertainties obtained over a period of 100 days for the induced cascade polarization are illustrated in Fig. 22 (left). Expected statistical significance for the model separation at the same W-bin as a function of experiment duration is shown in Fig. 22 (right). In this particular case, a 100 days experiment would reach a decisive level of 7.6 σ separation power, compared to only a 3.5 σ separation after 20 days.
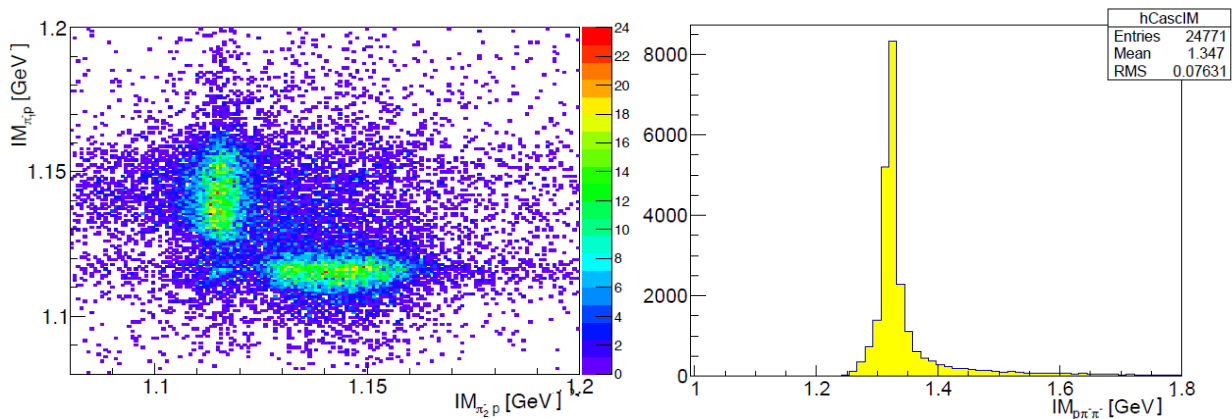
FIG. 21: <u>Left panel</u>: Invariant mass of detected proton and π_1^- as a function of Invariant mass of detected proton and π_2^-. <u>Right panel</u>: Invariant mass of detected proton and two π^-.
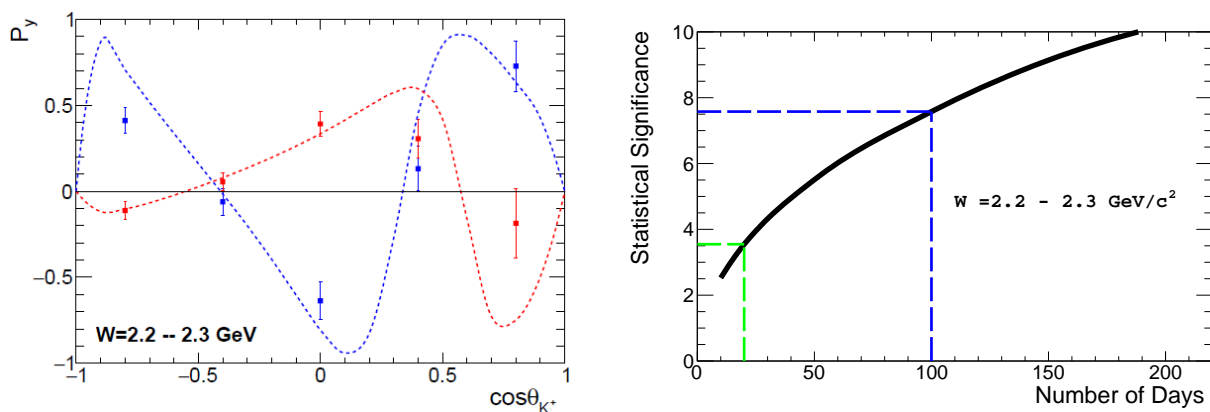

FIG. 22: <u>Left panel</u>: Estimated statistical uncertainties of the induced polarization of the Ξ^- in a $K_L n \to K^+ \Xi^-$ reaction as a function of CM $\cos\theta_{K^+}$ (two-fold differential). The curves show the theoretical predictions based on two solutions as described in Ref. [1]. <u>Right panel</u>: Expected statistical significance, in units of σs, to distinguish two models as a function of the running time. Two benchmark cases of 20 and 100 days are highlighted by the dashed green and blue curves, respectively.

It is evident that the determination of P_y will place very stringent constraints on the available models. The statistical uncertainties obtained over a period of 100 days are sufficient to investigate the underlying dynamics and cleanly differentiate between leading theoretical predictions.

The exclusivity of the reaction allows us to obtain a much cleaner sample of events with minimal background contributions. This will be done by requiring the invariant mass of the proton and the two negative pions to be consistent with the mass of Ξ^-. An additional requirement that the invariant mass of the proton-pion pair be consistent with the mass of the Λ will eliminate any background contributions other than the excited cascade channels. Contributions from excited cascade states can also be identified and removed by the application of coplanarity cuts between the strange meson and reconstructed cascade. Excited cascade states $K_L n \to K^+ \Xi^{-*}$ can also be identified, isolated, and studied in detail using the missing-mass technique assuming the target nucleon at rest.

VIII. $\mathbf{K_L n \to K^+ \Xi^{*-}}$:

The spectrum of excited cascades is barely known and practically nothing is known about their quantum numbers (see Ref. [1] (Chapter 3.1) for theory overview). To understand the ability of the KLF to contribute in this field, we have performed a series of simulations. The production of Cascades is always accompanied with kaons (K^+ or K^0) due to strangeness conservation. We have concentrated on reactions with the K^+ only to avoid unnecessary complications arising from the K^0 secondary decay vertexes. With K_L beam and associated K^+ one can produce either Ξ^{*0} on a proton target ($K_L p \to K^+ \Xi^{*0}$) or Ξ^{*-} on a neutron target ($K_L n \to K^+ \Xi^{*-}$). In both cases, the Ξ^* properties are
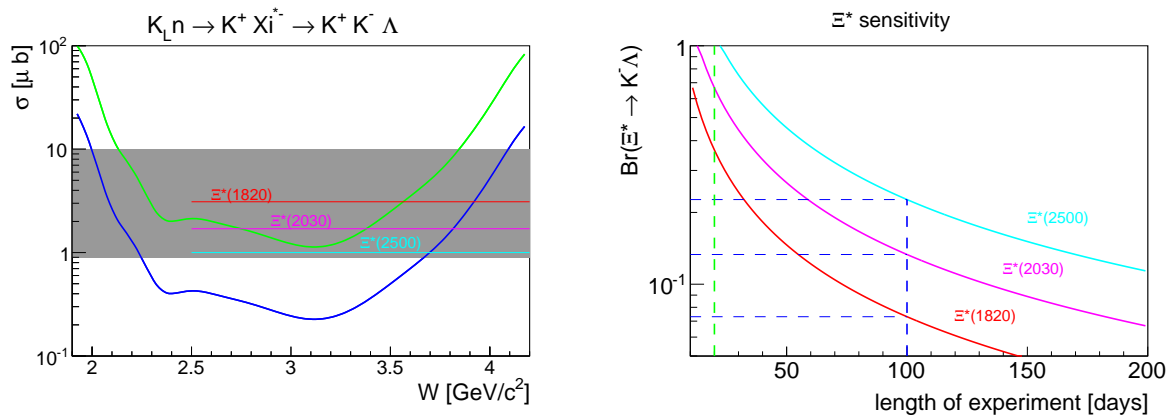
FIG. 23: <u>Left panel</u>: The Ξ^* discovery potential achievable at KLF during the 100 (blue) and 20 (green) day experiment, under assumption of 10 % statistical accuracy and $Br(\Xi^* \to \bar{K}\Lambda) = 1$. The gray band corresponds to typical Ξ^* cross sections and horizontal lines are few examples of BNL cross sections from Ref. [10] <u>Right panel</u>: Estimation of lowest measurable $\Xi^* \to \bar{K}\Lambda$ branching fraction at KLF as a function of experiment duration at W~$\overline{3.100\pm0.025}$ GeV. Two benchmark cases of 100 (20) days are highlighted by dashed blue (green) curves.

reconstructed from the final-state particles; hence, any minor differences due to the spectator momentum do not play any role. A dominant Ξ^{*-} decay branch is $\Xi^* \to \bar{K}\Lambda$. The Ξ^{*-} production looks more attractive since it has direct $\Xi^{*-} \to K^-\Lambda \to K^-p\pi^-$ decay with only one detached vertex from Λ decay. The full reaction contains four particles in the final state $K_Ln \to K^+\Xi^{*-} \to K^+K^-p\pi^-$ all of different types, which simplifies the analysis. Two negative pions - one from the Λ decay and one from the $\bar{K}^0$ and an extra detached vertex sufficiently complicates the analysis of this branch on proton target. Here we will present only the simplest case $K_Ln \to K^+\Xi^{*-}$ leaving other options for future studies.

The energy dependence of the $K_LN \to K^+\Xi^{*-}$ is not known. From the BNL measurements given in Ref. [10], we know that the Ξ^{*-} production cross section should be on the order of $1-10 \ \mu b$ – the higher the Ξ^* mass the lower the cross section, from $3.7\mu b$ for the $\Xi^*(1820)$ to $1\mu b$ for the $\Xi^*(2500)$. Some exotic cascades might have even lower production cross sections. We have tried to evaluate what Ξ^* production cross sections that might be measurable at K_L-facility within 20 and 100 days. We consider a lower bound of 10 % statistical uncertainty for the Ξ^* states to be identified. The results of our analysis can be seen in Fig. 23 in comparison with typical Ξ^* cross sections from Ref. [10]. From $N^* \to \pi N$ studies, it is known that for the high mass N^* states the $N^* \to \pi N$ branch get suppressed in favour of multi-pion ladder decays. A similar effect is expected to be seen for the high-mass Ξ^*. According to PDG [8], the $\Xi^* \to \bar{K}\Lambda$ is "dominant" for many Ξ^* states, however, we need to be prepared to measure somewhat suppressed $\Xi^* \to \bar{K}\Lambda$ decay of heavy Ξ^*'s. A W-variation of the Ξ^* production cross-section provide and important information on $\Xi^* \to \bar{K}\Lambda^*$ and $\Xi^* \to \bar{K}\Sigma^*$ couplings as an inverse process allowing further insight into Ξ^* internal structure.

<u>To summarize</u>: with 20 days beamtime one can barely touch the lowest-lying Ξ^* resonances keeping quantum numbers determinations, which requires precise measurements of the differential observables and Λ recoil polarization, out of consideration. With 100 days beamtime, all Ξ^* resonances could be measured with a statistical significance sufficient not only for the determination of mass and width parameters but also for spin-parity assignments as well.

IX.   DETAILS OF MC STUDY FOR $K_L p \to K^+ n$

The $K_L^0 p \to K^+ n$ reaction is a very special case in kaon-nucleon scattering. Due to strangeness conservation, formation of intermediate resonances is forbidden for this reaction. The main contribution comes from various non-resonant processes, which can be studied in a clean and controlled way. Similar non-resonant processes can be seen in other reactions where they can interfere with hyperon production amplitudes, causing distortion of the hyperon signals. That is why knowledge of the non-resonant physical background is important not only for the kaon-induced reactions but for all reactions with strangeness. The non-resonant nature of the reaction does not guarantee the absence of bumps in the total cross section: kaons and/or nucleons can be excited in the intermediate stage, producing bumps in the total cross section.

The reaction $K_L^0 p \to K^+ n$ is simple and has a very high production cross section (see Fig. 24); nevertheless, data on this reaction are scarce. It is a bit simpler to perform a positive kaon beam scattering for the inverse reaction, however, the reaction on a neutron target involves final-state interactions that may complicate the analysis. That is why the inverse reaction is also not so well known. A fair amount of differential cross-section data are available in the range $0.5 < p_{K_L} < 1.5$ GeV/c, predominantly from bubble chambers (see Ref. [11]) and there are a few measurements at high momenta: $p_K = 5.5$ GeV/c [12], $p_K = 10$ GeV/c [13]. In the energy range $2 < W < 3.5$ GeV, which can be covered by the KLF experiment with very high statistics, there are no data on this reaction at all.
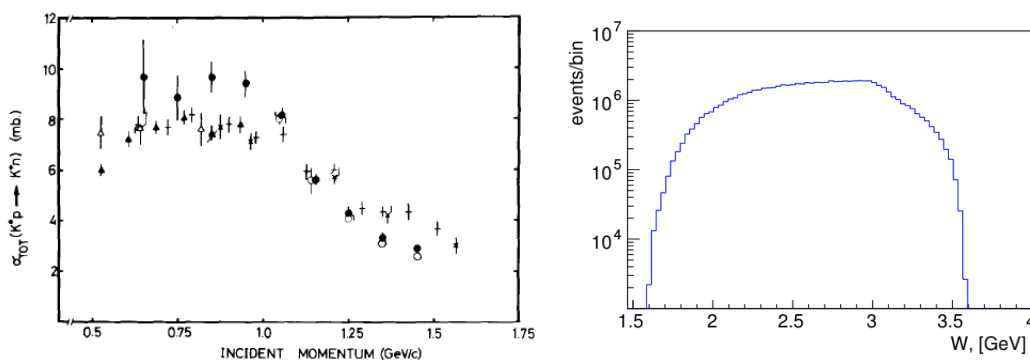

FIG. 24: Left: Total cross section for $K_L p \to K^+ n$ reaction as a function of K_L-momentum from Ref. [11]. right: Expected statistics for the $K_L p \to K^+ n$ after 100 days of measurement.

Detection of the charged kaon is enough to reconstruct the reaction fully via the missing-mass technique. If the beam energy is determined by ToF method utilizing the 24 m flight path between the kaon production Be-target and the reaction hydrogen target, the beam resolution is driven by the SC time resolution.

In addition to a kaon, one could also detect a neutron; however, due to poor neutron detection efficiency and the large systematic uncertainties associated with neutron detection, an improvement in the reconstruction of the reaction with this approach may be problematic. As described before, kaon identification is done with a probabilistic approach involving dE/dX, time-of-flight, and track curvature information. Even in pure $K_L p \to K^+ n$ MC case one can have more than one charged particle track reconstructed due to various reactions in the detector volume. That is why in addition to the pronounced K^+ banana in Fig. 25 (left) we see some traces of pion and proton bands. At low K^+-momenta, kaons can be well separated from pions and protons, but high-energy particles cannot be differentiated by dE/dX or by ToF information leading to particle misidentification. The higher W (the higher the ejectile energy), we have and the more kaons we lose due to misidentification; see Fig. 25 (right, green). In our analysis, we restricted ourselves to one and only one reconstructed charged-particle track. This condition helps to suppress the background, but does not reduce the reconstruction efficiency; see Fig. 25 (right, black).

Charged-particle track detection efficiency stays flat over the full range of W, but kaon reconstruction efficiency drops from about 60 % at low W to 20 % at W~3.5 GeV. Since the GlueX acceptance is large and essentially hole-less, kaon reconstruction efficiency does not depend on yet unknown angular distributions. For the final selection of the $K_L p \to K^+ n$ reaction, we used a 3σ missing-mass cut around the neutron's mass; see Fig. 26.

Figure 26 was plotted under the assumption of a 250 ps vertex time resolution. Both W (Fig. 24) and missing-mass resolutions are driven by the K_L-momentum resolution.

Below W = 2.4 GeV, the $K_L p \to K^+ n$ and $K_L p \to K^+ \Xi$ reactions can be disentangled by K^+ missing mass alone. Above this value, special treatment of the $K_L p \to K^+ \Xi$ background is required. One may notice that a 3σ cut for the $K_L p \to K^+ n$ reaction rises faster than for $K_L p \to K^+ \Xi^0$. This effect has a purely kinematical explanation - due to the higher mass of the Ξ^0 baryon, the K^+ produced in $K_L p \to K^+ \Xi$ reaction has a lower energy for the same
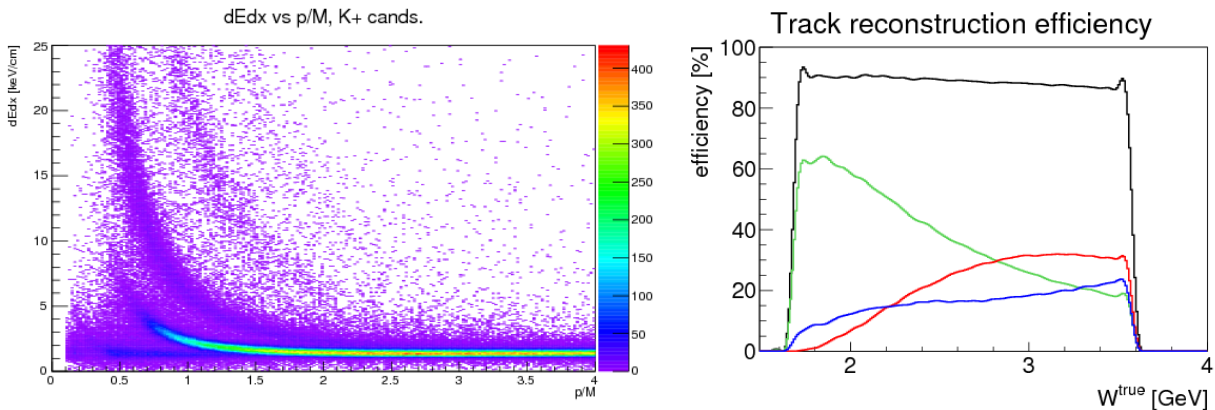
FIG. 25: Left panel: dE/dx for the $K_L p \to K^+ n$ channel. Right panel: Single charged-particle track detection efficiency as a function of W for the $K_L p \to K^+ n$ channel. Any charged particle (black), kaon (green), proton (red), and pion (blue).
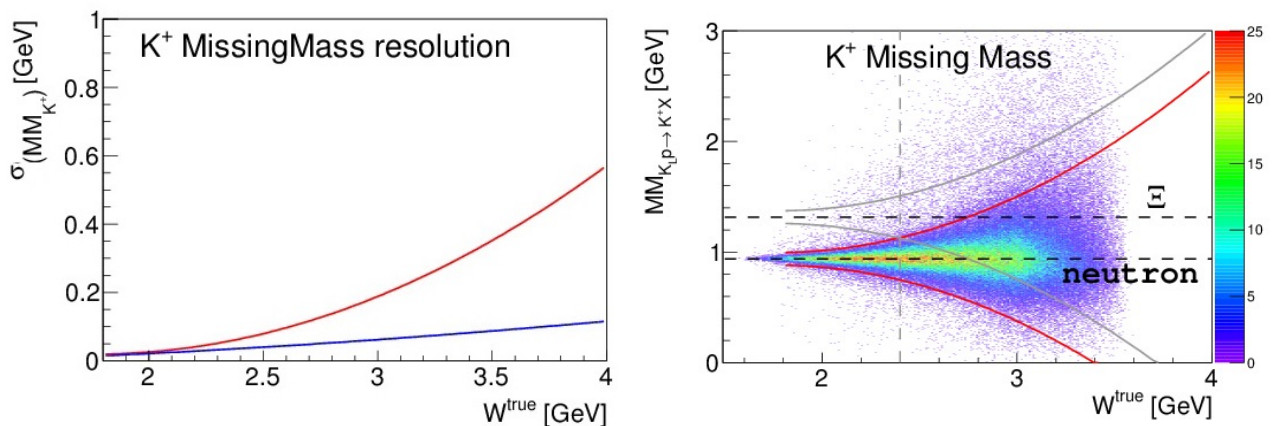

FIG. 26: Left panel: Full (red) and detector related (blue) K^+ missing-mass resolution in terms of σ. In second case, the true K_L-momentum was used to calculate the missing mass. Right panel: K^+ missing-mass resolution as a function of W. 3σ missing-mass cuts for the $K_L p \to K^+ n$ (red) and $K_L p \to K^+ \Xi$ (gray) reactions are indicated by solid lines. Horizontal dashed lines show nominal masses of the neutron and Ξ baryon. The vertical gray dashed line indicates the range of pure missing-mass separation between these two reactions.

value of W. The lower the K^+ energy we have, the better missing-mass resolution we get, and the more narrow the missing-mass cut one needs to apply.

With the simulation performed, we determine that in 100 days of a beamtime, around 60M $K_L p \to K^+ n$ events will be detected. A typical example of the expected statistics in comparison to previous data are shown in Fig. 27 (left). The highest flux is expected around $W = 3$ GeV, where we had to increase statistical uncertainties by a factor of 10 to make them visible (see Fig. 27 (right)).

There are three major sources of background: $np \to K^+ nn$, $np \to \pi^+ nn$, and $K_L p \to K^+ \Xi^0$. Neutron flux drops exponentially with energy and generally the high-energy neutron flux is tiny.

A. $K_L p \to K^+ n$ Background Suppression:

Due to its very high cross section, the $K_L p \to K^+ n$ reaction is essentially background free. Due to the extremely high statistics expected for this reaction our uncertainties will be dominated by systematics. We have identified three major sources of physical background: $np \to K^+ nn$, $np \to \pi^+ nn$, and $K_L p \to K^+ \Xi$ reactions.

Details on $K_L p \to K^+ n$ and $K_L p \to K^+ \Xi$ separation can be found in Section VII. For $W < 2.3$ GeV, these two reactions can be separated by a 3σ K^+ missing-mass cut. Above W = 2.4 GeV, one can use standard background suppression techniques - S-weights, Q-weights, NeuralNets, etc. .... The main decay branch of Ξ is $\Xi^0 \to \pi^0 \Lambda \to$
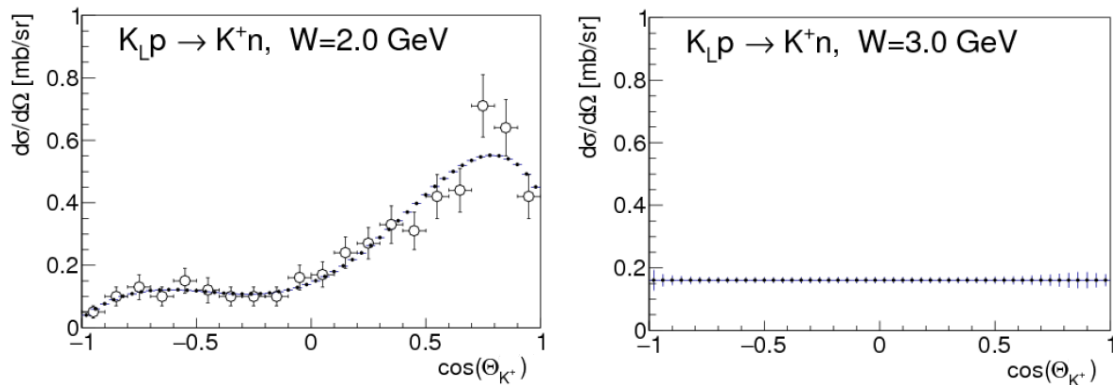
FIG. 27: Left panel: Cross-section uncertainty estimates (statistical only) for $K_L p \to K^+ n$ reaction for the $W = 2$ GeV in comparison with data from Ref. [11]. Right panel: Same distribution for the $W = 3$ GeV. The error bars for the right plot were increased by factor of 10 to make them visible.

$\pi^0 \pi^- p$, which leads to several charged particles in the final state besides K^+; hence filtered out by a "one-charge-track-only" selection criterion. Another decay branch $\Xi^0 \to \pi^0 \Lambda \to \pi^0 \pi^0 n$ cannot be filtered out that easily; however, due to its smaller branching ratio combined with the small $K_L p \to K^+ \Xi$ production cross section, this channel only contributes at the level of 10^{-3} even without any background suppression techniques. Further suppression vetoing multiple neutral tracks and/or Q-weight should push this background far below 10^{-4}.

Neutron flux drops exponentially with energy and generally the high-energy neutron flux is small, but nonvanishing. If neutrons and K_Ls have the same velocity, they cannot be separated by time of flight. Neutron-induced reactions have high cross sections, which is why one needs to consider them as a possible source of background. In Fig. 28 (left), one can see a comparison of kaon and neutron fluxes in terms of β for the worse-case scenario when no neutron suppression is employed. Particles with the same β cannot be separated by time-of-flight. At $\beta = 0.95$ neutron and kaon fluxes become equal. This velocity corresponds to a neutron momentum of $p_n = 2.9$ GeV/c and kaon momentum of $p_K = 1.5$ GeV/c.
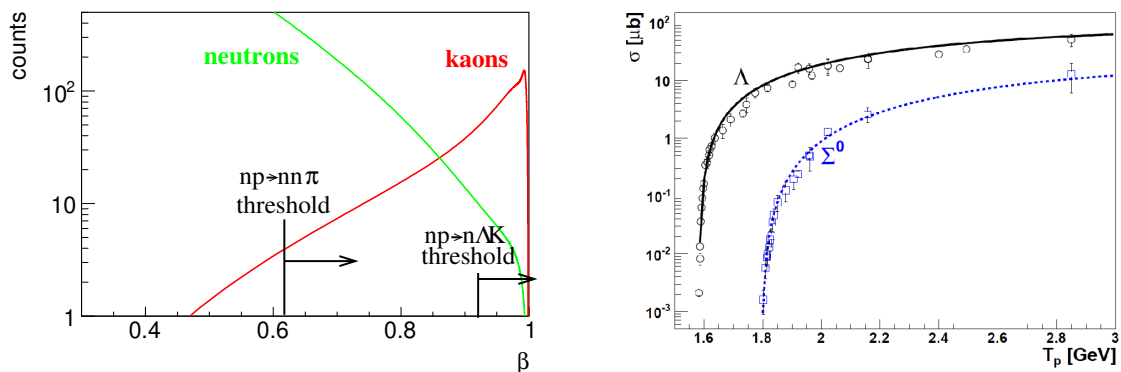

FIG. 28: Left panel: Neutron and K_L fluxes as a function of velocity β. Right panel: $pp \to K^+ \Lambda p$ total cross section from Ref. [14].

To evaluate the amount of background, we need to fold this flux with production cross section and reconstruction efficiency. Let's first consider the $np \to K^+ \Lambda n$ background. Unfortunately, this reaction is not very well measured, so we would use the $pp \to K^+ \Lambda p$ cross section parametrization together with the knowledge of $\frac{\sigma(pp \to K^+ \Lambda p)}{\sigma(np \to K^+ \Lambda n)} = 2$ from Ref. [14]. In Fig. 29, one can see the flux of K^+s from kaon-induced $K_L p \to K^+ n$ reaction in comparison to a neutron-induced $np \to K^+ \Lambda n$ as a function of projectile velocities.

As one can see in Fig. 29, neutron-induced K^+ production contributes only in a very narrow range of energies. The contribution is also very small. One can further suppress this type of background by vetoing charged particles from Λ decay and performing a K^+ missing-mass cut. Altogether one can suppress this type of background below 10^{-4}.

The most dangerous type of neutron-induced background originates from the $np \to \pi^+ nn$ reaction with fast π^+
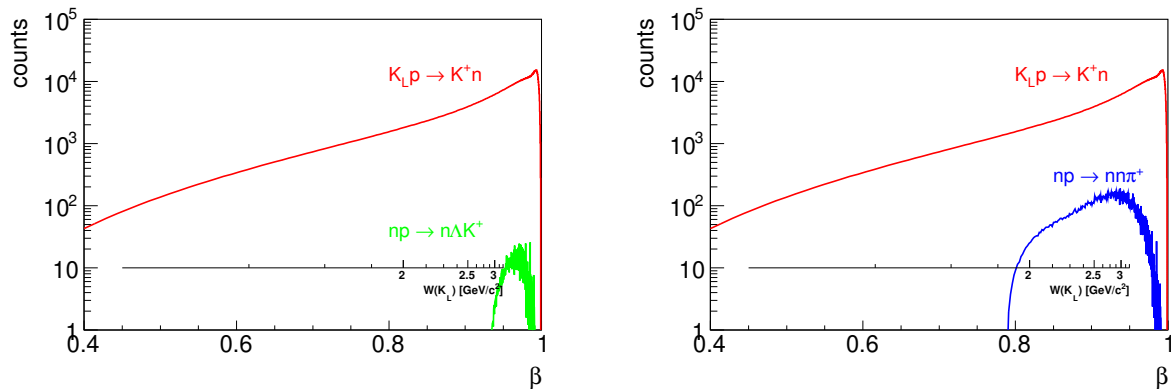
FIG. 29: Left panel: K^+ flux as a function of projectile velocity β for neutron-induced (green) and kaon-induced (red) reactions. Right panel: same but for $np \to \pi^+ nn$ (blue) and $K_L p \to K^+ n$ (red) reactions. Pion misidentification efficiency for the neutron-induced reaction is extracted from the full MC Geant simulation. Secondary axis showed corresponding W value under assumption of $K_L p \to K^+ n$ reaction.

misidentification as K^+. There are no measurements of $np \to \pi^+ nn$ reaction but due to isospin symmetry one can relate this reaction to an isospin symmetric case $np \to \pi^- pp$. The later reaction is known, see Ref. [15]. The total cross section for this reaction is about 2 mb. The $np \to \pi^+ nn$ reaction has a much lower threshold compared to $np \to K^+ \Lambda n$, so it can utilize an enormous flux of low-energy neutrons. However, low-energy neutrons predominately produce low-energy pions, which can be separated from kaons. The background needs to be considered only for $\beta > 0.8$; see Fig. 29 (right). The background level looks much higher compared to Fig. 29 (left), but it can be severely suppressed with the "K^+" missing-mass cut since pion kinematics of the three-body $np \to \pi^+ nn$ reaction is very different from the $K_L p \to K^+ n$.

To summarize: Kaon particle identification together with a simple 3σ missing-mass cut and assumption of K_L beam can efficiently suppress all physical backgrounds of the $K_L p \to K^+ n$ reaction.

X. PHOTON BACKGROUND

Due to extended beryllium target and tungsten plug the photon background at the face of $LH2/LD2$ target is small. A further suppression of photoinduced reaction originates from the weakness of electromagnetic interaction compare to strong. In Fig.30 (left) one can see the expected photon flux as a function of energy. By folding it with a photoproduction cross-section Ref. [16] one can get expected countrate from the photoproduction, Fig. 30(right). Overall countrate is expected to be 3.8 events per second - less than 4Hz. With such a low countrate no special treatment is required for the photon background neither at trigger level nor at analysis.
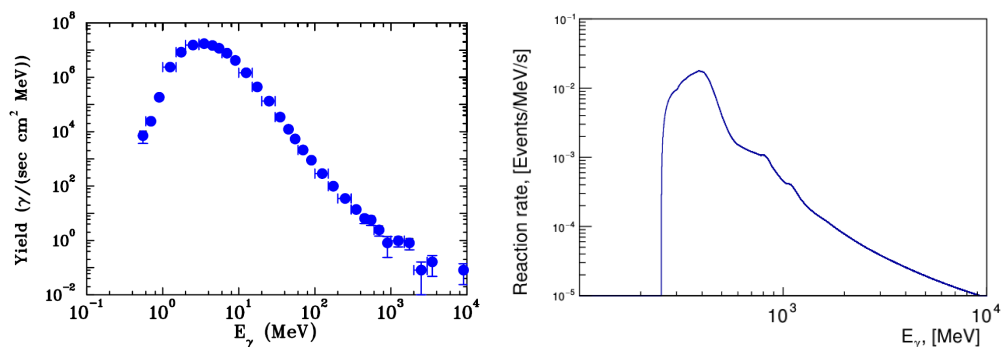

FIG. 30: Left panel: Photon flux at the $LH2/LD2$ target as a function of energy. Right panel: Expected countrate for the photoproduction reactions as a function of energy

[1] *Strange hadron spectroscopy with secondary K_L beam in Hall D*, Spokespersons: M. J. Amaryan, M. Bashkanov, S. Dobbs, J. Ritman, J. R. Stevens, and I. I. Strakovsky (KLF Collaboration), JLab C2–19–001, Newport News, VA, USA, 2019.

[2] H. Seraydaryan *et al.* [CLAS Collaboration], "ϕ-meson photoproduction on Hydrogen in the neutral decay mode," Phys. Rev. C **89**, no. 5, 055206 (2014).

[3] S. Adhikari *et al.* [GlueX Collaboration], "The GlueX beam line and detector," in progress.

[4] E. Pooser *et al.*, "The GlueX Start Counter Detector," Nucl. Instrum. Meth. A **927**, 330 (2019).

[5] T. D. Beattie *et al.*, "Construction and Performance of the Barrel Electromagnetic Calorimeter for the GlueX Experiment," Nucl. Instrum. Meth. A **896**, 24 (2018).

[6] H. Al Ghoul *et al.* [GlueX Collaboration], "First Results from The GlueX Experiment," AIP Conf. Proc. **1735**, 020001 (2016).

[7] P. Capiluppi, G. Giacomelli, G. Mandrioli, A. M. Rossi, P. Serra-Lugaresi, and L. Zitelli, "A COMPILATION OF K0(L) p CROSS-SECTIONS," IFUB-81-25.

[8] M. Tanabashi *et al.* [Particle Data Group], "Review of Particle Physics," Phys. Rev. D **98**, no. 3, 030001 (2018).

[9] R. Yamartino *et al.*, "A Study of the Reactions anti-K0 p —¿ Lambda pi+ and anti-K0 p —¿ Sigma0 pi+ from 1-GeV/c to 12-GeV/c," Phys. Rev. D**10**, 9 (1974); Ph. D Thesis, SLAC Standford University, 1974; SLAC–R–0177, SLAC–R–177, SLAC–0177, SLAC–177.

[10] C. M. Jenkins *et al.*, "Existence Of Xi Resonances Above 2-GeV," Phys. Rev. Lett. **51**, 951 (1983).

[11] J. C. M. Armitage *et al.*, "A Study of K0 p Charge Exchange Scattering from 0.6-GeV/c to 1.5-GeV/c," Nucl. Phys. B **123**, 11 (1977).

[12] D. Cline, J. Penn, and D. D. Reeder, "The k+ n charge-exchange reaction at 5.5 GeV/c," Nucl. Phys. B **22**, 247 (1970).

[13] P. Bajllon *et al.*, Nucl. Phys. B **134**, 31 (1978).

[14] Y. Valdau *et al.*, "Comparison of inclusive K^+ production in proton-proton and proton-neutron collisions," Phys. Rev. C **84**, 055207 (2011).

[15] P. Adlarson *et al.* [WASA-at-COSY Collaboration], "Isoscalar Single-Pion Production in the Region of Roper and $d^*(2380)$ Resonances," Phys. Lett. B **774**, 599 (2017).

[16] B. Krusche, Prog. Part. Nucl. Phys. **55**, 46 (2005).